Process Compensated Resonance Testing Models for Quantification of Creep Damage in Single Crystal Nickel-Based Superalloys

Julieanne V. Heffernan*, Leanne Jauriqui†, Eric Biedermann‡, Alexander Mayes§, Richard Livings¶, Brent Goodlet**, Siamack Mazdiyasni††

ABSTRACT

Process compensated resonant testing (PCRT) is a full body nondestructive evaluation (NDE) method that measures the resonance frequencies of a part and correlates them to the part's material state, structural integrity, or damage state. This paper describes the quantification of creep damage in a virtual part population via the correlation of PCRT parameters to creep strain using inversion methods and vibrational pattern recognition (VIPR) analysis. Modeled populations were created using the finite element method (FEM) for single crystal (SX) nickel-based superalloy dogbone and turbine engine airfoil geometries. The modeled populations include nominal variation in crystallographic orientation, geometric dimensions, and material properties. Modeled populations also include parts with variable levels of creep strain, allowing for NDE sensitivity studies. FEM model inversion tools quantified creep strain and distinguished it from other variations in the part populations. Resonant modes that were found to be particularly sensitive to creep strain were evaluated using VIPR algorithms to correlate and quantify creep strain with PCRT metrics. The results for PCRT forward models, model inversion, and VIPR correlations were verified with experimental creep strain measurements made for dogbone specimens. This verification demonstrated that PCRT inspections can be trained through forward models to detect and quantify creep damage in a part.

KEYWORDS: creep, PCRT, resonance, forward modeling, inversion, NDE, nickel-based superalloy.

* Vibrant Corporation, 8330 Washington Pl. N.E., Albuquerque, New Mexico, 87113-1674; (575) 418-0890; jheffernan@vibrantndt.com
† Vibrant Corporation, 8330 Washington Pl. N.E., Albuquerque, New Mexico, 87113-1674; (575) 418-0890; ljauriqui@vibrantndt.com
‡ Vibrant Corporation, 8330 Washington Pl. N.E., Albuquerque, New Mexico, 87113-1674; (575) 418-0890; ebiedermann@vibrantndt.com
§ Vibrant Corporation, 8330 Washington Pl. N.E., Albuquerque, New Mexico, 87113-1674; (575) 418-0890; amayes@vibrantndt.com
¶ Vibrant Corporation, 8330 Washington Pl. N.E., Albuquerque, New Mexico, 87113-1674; (575) 418-0890; amayes@vibrantndt.com
** University of California, Santa Barbara, Materials, E-II Bldg. 503, Rm. 1355, Santa Barbara, California; (720) 291-5613; brent.goodlet@gmail.com
†† Air Force Research Laboratory (AFRL/RXCA), Bldg. 655, Rm. 18, Wright-Patterson AFB, Ohio; siamack.mazdiyasni@us.af.mil

Introduction

Process compensated resonant testing is a full body nondestructive evaluation method that uses multiple resonance frequencies of a part to evaluate its structural integrity and material states (ASTM, 2016). PCRT combines resonant ultrasound spectroscopy (RUS) (Migliori et al., 1993), pattern recognition analysis, and statistical scoring of frequency data to perform pass/fail (P/F) NDE, process monitoring, life monitoring, and material characterization for commercial and scientific applications (Schwarz et al., 2005). One of the most critical applications is the evaluation of gas turbine engine airfoils made from nickel-based superalloys (Piotrowski et al., 2008). Prior work on nickel-based superalloy gas turbine airfoils has shown PCRT capable of measuring shifts in resonance frequency peaks which are correlated with high temperature exposure (Piotrowski et al., 2008; FAA, 2010). Additionally, the NDE potential gained from coupling forward finite element method (FEM) models of incrementally crept dogbones to the PCRT measured changes in resonance resulting from creep strain was explored for polycrystalline nickel-based superalloy dogbones (Goodlet et al., 2017; Biedermann et al., 2016).

PCRT applications use a training set consisting of components that represent the range of acceptable process variation—one or more defective conditions—as well as the range of severity in those defective conditions. The VIPR algorithms use this training set to identify the most diagnostic resonances for the condition(s) of interest (Jauriqui, 2010). VIPR readily

identifies parts with resonance differences due to a defect, however, it has not frequently been used to characterize or quantify defects. Additionally, a significant number of targeted defective samples are often hard to obtain from a service population or are too costly to create experimentally. Forward modeling in PCRT has the potential to greatly increase the method's material characterization capability while reducing the need for large training populations of physical samples (Biedermann et al., 2016).

PCRT inversion tools have been expanded to use the mechanical resonances of a part to simultaneously estimate varying material properties and changes in part geometry. The capability of performing inversion using surrogate models from FEM simulations has also been developed, addressing crystal orientation and complex geometries (Biedermann et al., 2016). Work continues towards the goal of using inversion tools to identify the type and severity of damage, on a path toward identifying structural deficiencies with greater confidence. Further development of these NDE tools holds the promise of reduced risk of in-service component failure, and extension of serviceable component lifetimes due to reduced uncertainty in life estimates.

This work explores the quantification of creep damage in a virtual part population via the correlation of PCRT parameters to creep strain using inversion methods and VIPR analysis. FEM modeled design spaces of single crystal (SX) nickel-based superalloy samples for dogbone and turbine blade geometries were created. Design spaces included models with nominal levels of variation in crystallographic orientation, geometric dimensions, and material properties. The design spaces also included models with excessive plastic deformation to simulate creep strain. FEM inversion tools are then demonstrated to successfully quantify creep strain from natural parameter variations in the modeled part population. With diagnostic modes found to be sensitive to creep strain using VIPR algorithms, quantification of creep strain is also demonstrated using traditional PCRT metrics. Finally, inversion methods were verified with experimental data collected from a SX dogbone crept incrementally. This work demonstrates that FEM inversion and VIPR algorithms can be trained through PCRT forward models to invert the quantity of creep damage in a part.

Methods

Finite-Element Method Forward Modeling of Creep

A series of populations were created using FEM software for SX superalloy dogbones and turbine blade geometries for the purpose of developing virtual training sets of acceptable and nonacceptable parts accounting for expected population variances of geometric, material, and defect creep elongation parameters. Forward models were generated through FEM. Modeling the shape change associated with creep was accomplished with a nonlinear plastic analysis, which is generally more straightforward than a full creep plasticity analysis and should yield very similar deformation characteristics. Deformation of SX material required an anisotropic (cubic) elastic/plastic material model using a Hill stress potential function as detailed by other scholarship (Ramaglia and Villari, 2013; Biedermann et al., 2017). After each creep strain interval was modeled, the deformed shape was imported into an FEM modal analysis, using a block lanczos eigensolver, to predict the change in resonance frequencies resulting from creep strain accumulation.

Forward model parameters of the 10 mm gage length SX dogbone have been previously reported (Biedermann et al., 2015), including dimensional variation in gage length, elastic properties, crystallographic orientation, and accumulated creep strain. To create a PCRT forward model sensitivity study of creep for a more complex geometry, a 54 mm long turbine blade with an internal cooling passage was also represented using models (Grabcad, 2016). Figure 1 shows the dogbone and blade models. In the blade geometry the root volume was fixed and a body force was applied to simulate the boundary conditions and centripetal loads the blade could experience in service. The angle (θ) between the (001) crystallographic axis (Z') and the long axis of the airfoil (Z) was varied to capture normal variation and potential casting defects in grain orientation. To simulate the deformed geometry associated with creep, the load applied to the airfoil was adjusted to produce varying levels of nonlinear plastic strain as measured along the trailing edge of the blade.

A series of one-factor-at-a-time (OFAT) studies varied each geometric, material, and creep parameter individually to evaluate its effect on resonance variation and establish a normal distribution of parameters within the ranges specified. Next, monte carlo (MC) simulations randomly selected parameter values from within the specified ranges and generated FEM models to simulate the frequency profiles produced by the monte carlo parameterization. Then, a selection of normal design points were modeled with varying amounts of creep strain. Table 1 describes the parameters and their ranges chosen for the single crystal blade monte carlo design spaces.

Previous results have quantified the overall uncertainty in resonance frequencies resulting from coupled variation in geometry, material properties, crystallographic orientation, and creep damage for nickel-based superalloys (Biedermann et al., 2017). For instance, error can be introduced with inaccurate mode shape tracking. Each resonance mode has both a characteristic frequency and mode shape, or pattern, in which the part oscillates as it resonates. For inversion interpolations to produce meaningful results, proper mode alignment between the two FEM model runs is essential. However, this process is complicated by the fact that changes in any parameter value can affect the ordering in which resonance modes appear in the frequency regime. This mode-swapping requires a robust mode shape based tracking and matching of modes.

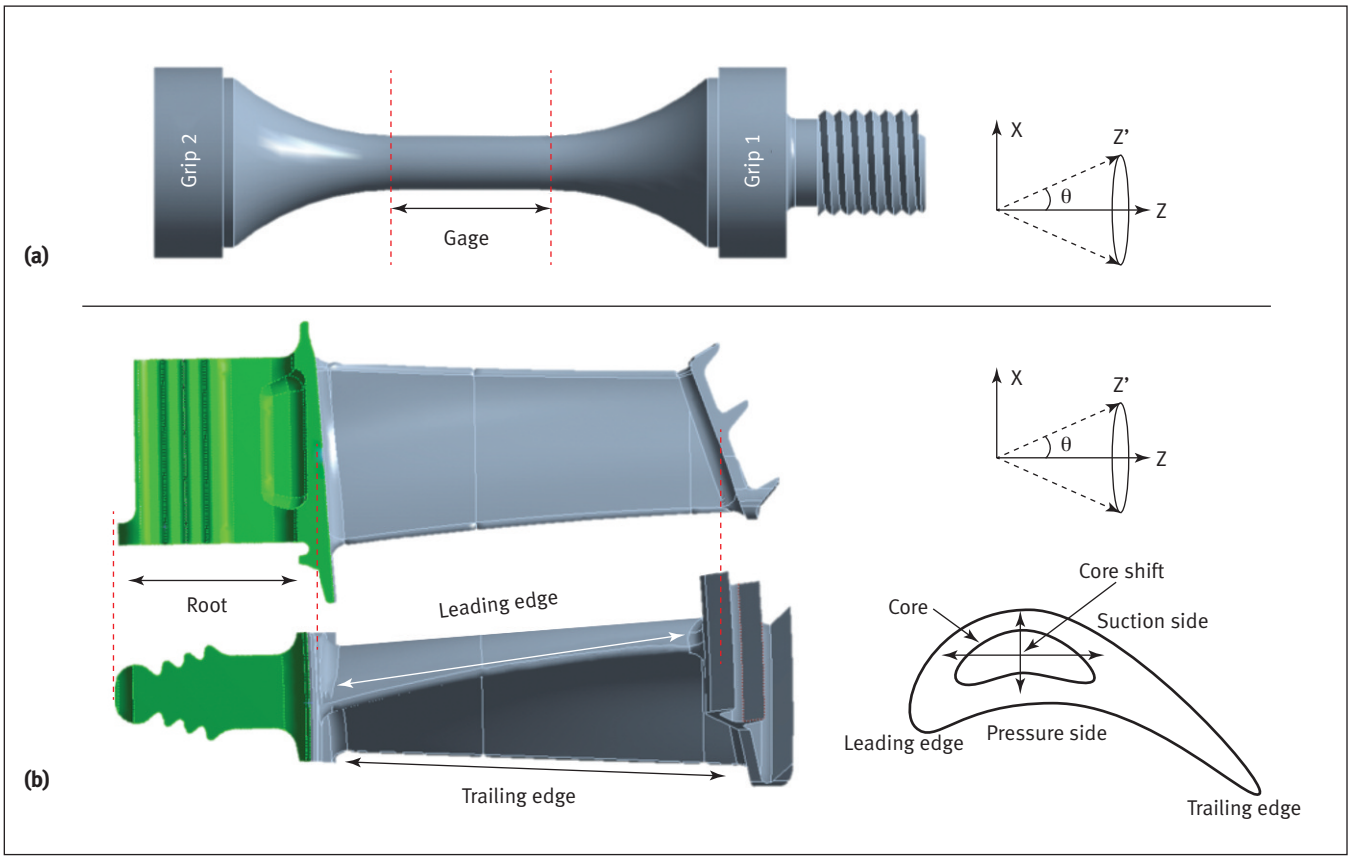

Figure 1. Diagrams: (a) dogbone geometry; and (b) and blade geometry. For each geometry, angle (θ) is defined between the (001) crystallographic axis (Z') and the long axis of the dogbone or airfoil (Z).

TABLE 1
Coupled parameters for the SX blade forward model Monte Carlo design space studies*

	Parameter description	Parameter range
Normal population: geometry	Airfoil thickness diameter	±0.02%
	Airfoil span	±0.04%
	Leading edge inflation/deflation	±0.01%
	Trailing edge inflation/deflation	±0.01%
	Core thickness diameter	±0.04%
	Twist/untwist of airfoil	±2.6°
	Core shift	±0.1% leading edge to trailing edge, ±0.1% pressure to suction side
Normal population: material	Poisson ratio along crystal (001), ($\nu_{(001)}$)	±2%
	Young's modulus along crystal (001), ($E_{(001)}$)	±2%
	Anisotropy ratio, (A)	±3%
	Density	±0.2%
	Angle of (001) crystal axis rotation, (θ)	±15°
Defect population: geometry	Same as normal population	Ranges listed above
Defect population: material	Added creep strain, as measured along trailing edge	0.5–10%

* Geometric ranges represent estimates of acceptable design tolerance.

Mitigating mode matching error can be very difficult and often involves direct comparison of all the mode shapes in a design space. Fortunately, while resonance frequencies vary significantly within the possible parameter space, resonance mode shapes are much more consistent. Therefore, resonance modes for each simulation were matched according to a series of modal assurance criterion correlations, described in detail in other work (Pastor et al., 2012).

FEM Inversion Method for Creep

Historically, inversion has been used to estimate bulk material properties of parts with simple geometries (Migliori et al., 1993; Migliori and Sarrao, 1997). In order to estimate more complex material states and geometries, such as creep in a coupon or turbine blade, an FEM model-based inversion approach was chosen.

The purpose of inversion is to estimate a set of parameters describing a part, such as creep strain, from a measured set of the part's resonant frequencies. This is achieved using an iterative solving method, shown in Figure 2, wherein the user gives the measured frequencies and an initial guess of the parameters to an optimization routine. The optimization routine then passes the guessed parameters to a model, which outputs what the corresponding resonant frequencies should be. The modeled frequencies are compared to the measured sample frequencies and the optimization routine adjusts its parameter estimates based on the resultant error. This process is repeated until the resonance mode shape error is below a convergence threshold, at which point the current parameterization is returned as the best fit parameters.

The inversion process often requires many iterations to converge to a solution, and running a full FEM model run at each iteration could require hours, or even days, to complete a single inversion analysis. One way to decrease inversion time is to simulate a series of design points that spans the bounds of the parameters of interest and then create a metamodel that quickly interpolates between the generated frequencies.

The metamodeling approach described here is a gridded design space. It involves creating an *N*-dimensional evenly spaced grid of FEM design points and employing cubic spline interpolation for estimations between design points. Gridded design spaces offer good frequency estimates that increase in accuracy with resolution of the design space. However, they also require an exponential increase in the minimum number of design points generated with each additional inversion parameter, as well as significant increases in interpolation time. This makes gridded design spaces well suited for inversion problems with four or fewer parameters, while greater payoffs come from numerous inversion runs. Ultimately, the decision between conducting inversions from interpolated gridded design space data or performing FEM calculations on the fly must consider the likely number of inversion runs, the number of invertible parameters, the range of possible parameter values, and the desired resolution of each parameter being estimated.

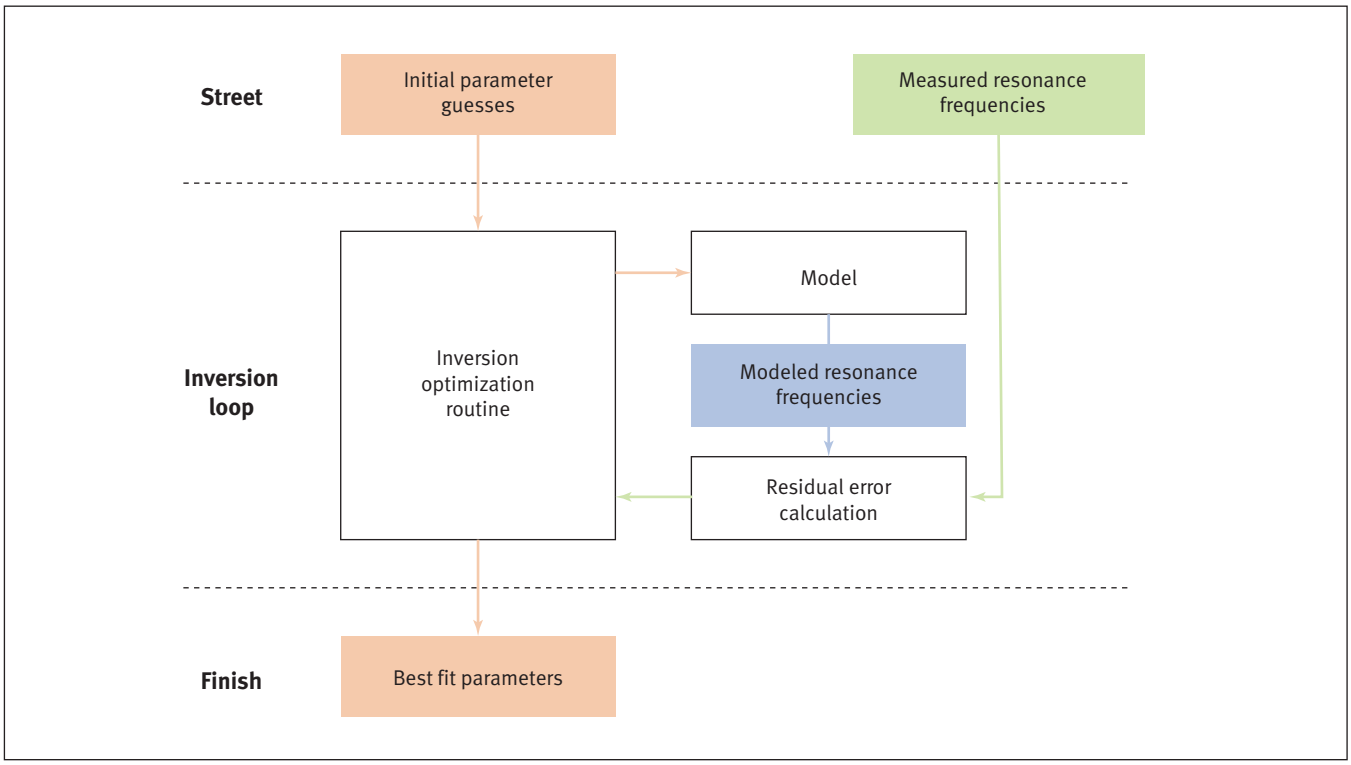

Figure 2. Flow diagram of the resonant ultrasound spectroscopy inversion process.

TABLE 2
Dogbone parameter ranges for material properties, dimensions, and creep strain used for inversion studies*

Parameter	Range	Minimum	Nominal	Maximum
E_{001}	±2%	125.2 GPa	127.7 GPa	130.3 GPa
ν_{001}	±7%	0.348	0.374	0.400
A	±5%	2.615	2.753	2.890
θ	0–10°	0°	0°	10°
Creep	0–8%	0%	0%	8%
Gage length	±1.00%	9.90 mm	10.0 mm	10.10 mm
Gage diameter	±0.75%	3.97 mm	4.00 mm	4.03 mm
Grip lengths	±1.11%	4.45 mm	4.50 mm	4.55 mm

* Creep deformation presented as % change in nominal gage length.

The inversion toolset used a gridded design space generated from forward models of dogbones that varied five material properties: elastic modulus (E_{001}), Poisson's ratio (ν_{001}), anisotropy ratio (A), crystal orientation (θ grain angle), and creep strain. In addition to the design space, several models were created that varied the material properties as well as the dimensional parameters of gage length, gage diameter, and grip length. The material and dimensional varied samples were used to gage the error in the inversion code caused by extra variation that was not in the gridded space. Table 2 provides nominal values and bounds for the gridded design space as well as the dimensional parameter bonds for the extra models.

VIPR Creep Correlation Method

VIPR is used to identify the resonance modes that are most sensitive to various conditions of interest, or are most diagnostic of defective conditions. Depending on the variation included in the acceptable and nonacceptable training sets, the diagnostic pattern will often include peaks that are sensitive to the defect, and some that are not. As such, VIPR focuses on the relationships and patterns between resonances, not the absolute frequencies themselves. Statistical scoring using the mahalanobis-taguchi system (MTS) calculates the mahalanobis distance which, in a PCRT context, is the measure of a part's position relative to the central tendency of the reference population in N-dimensional frequency space (Cudney, 2009). VIPR uses taguchi-based signal-to-noise methods to evaluate thousands of combinations of resonances from a database of candidates to discover the combination that best separates acceptable from defective parts using the MTS score (Taguchi et al., 2001; Schwarz et al., 2005).

While VIPR can easily identify resonance peaks sensitive to creep (Biedermann et al., 2016), it had not been used as an inversion tool to quantitatively evaluate the amount a specimen has been crept. In contrast with the direct inversion methods discussed in the preceding section, VIPR predictions require relatively few resonance measurements. In this study, forward model design spaces were used to train VIPR to separate modeled samples with creep strain, from modeled samples without creep damage. Then VIPR algorithms were used to identify combinations of diagnostic modes that produced the best correlations to creep damage. Once these modes were identified, a VIPR-based correlation tool for quantifying creep strain was established, and tested against modeled and measured PCRT data.

Experimental Creep on Single Crystal Dogbones: Inversion Validation

Iterative creep was performed on a SX dogbone in order to produce measured PCRT data for validation of forward models and to test the inversion methods discussed above. The single crystal dogbone had the same geometry as described in other works (Biedermann et al., 2016), while the experimental procedures employed were similar to those described in previous work on creep of polycrystalline superalloy dogbones (Goodlet et al., 2017). First the dogbone was affixed to the load frame, gripping the sample by a recessed ledge just beyond the gage and filleted regions. A clam-shell furnace enclosed the sample and the specimen grips, and was used to heat the dogbone to 950 °C. Once the furnace temperatures stabilized at the target temperature, a uniaxial load of 300 MPa was applied and extensometer readings began. Two digital extensometers attached to a creep-resistant scaffolding aligned to the dogbone grips recorded the elongation of the dogbone for the duration of the test. When the desired amount of creep strain had accumulated, the test stopped by unloading the specimen and opening the clam-shell furnace for cooling in air. Using this procedure, a single dogbone was iteratively crept for a total of approximately 14% strain, as measured from the original 10 mm gage length. After each creep step the dogbone was cooled to room temperature, measured with calipers to verify the extensometer readings, and evaluated with PCRT. Both the VIPR and FEM inversion approaches were then used to quantify the creep elongation experienced by the dogbone based on its measured resonance response.

Results and Discussion

FEM Forward Modeling of Creep

Over 300 dogbone and 250 blade MC-generated design points, with and without creep, were simulated. A baseline model with nominal values and zero creep strain was established for each specimen geometry. The first 50 resonance modes of subsequent model runs were mode matched to align with the established baseline mode order. Combining these subsequent model runs, each with unique MC parameterizations, resulted in a diverse population of modeled results for inversion estimation and VIPR training.

The modeling results for SX dogbones were presented by another author (Biedermann et al., 2015). Unlike the uniaxial plastic strain deformation seen in the creep of the SX dogbone samples (Biedermann et al., 2016), the blades do not deform in a purely axial manner, as shown in Figure 3, due to their complex geometry. However, in both the dogbone and blade geometries, increasing creep strain often produced a decrease in frequency for the sensitive resonance modes. Of the modes identified as diagnostic modes substantially affected by accumulation of creep strain, lower-frequency modes exhibiting bending motions were most common.

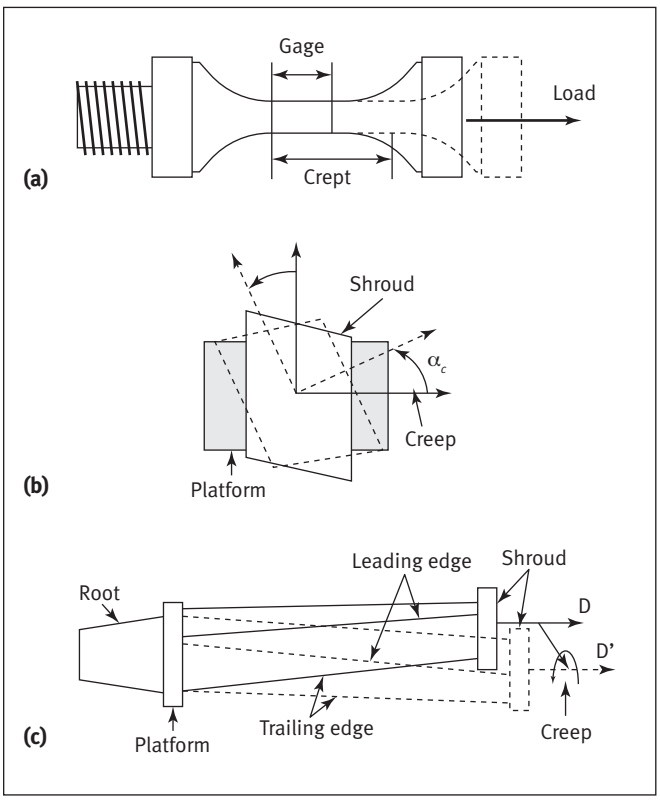

Figure 3. Sample dimensions depicted before creep strain was applied (solid), and after (dashed): (a) axial deformation of an SX dogbone; (b) twisting deformation ($\propto_c$); and (c) bending deformation along the long axis (D to D') in a turbine blade.

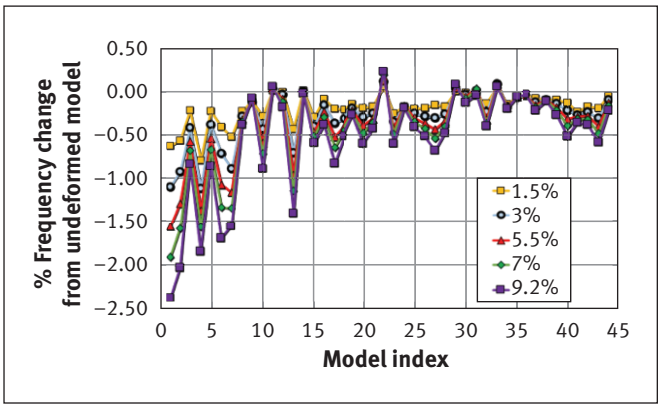

Figure 4. One-factor-at-a-time results for changes in resonance frequencies of a simulated blade with increasing creep strain.

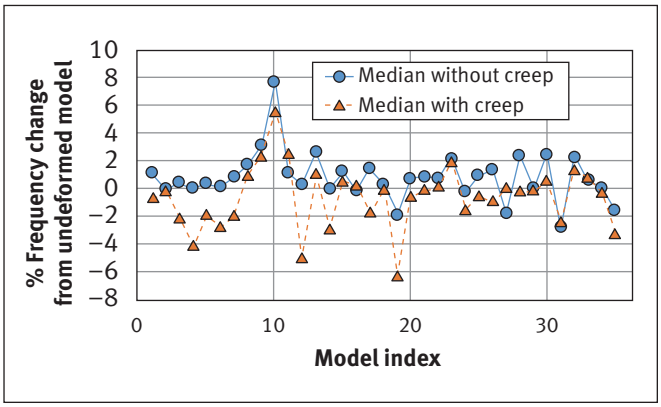

Figure 5. Median variation of model frequencies in the blade monte carlo populations, with creep (dashed orange line) and without creep (solid blue line).

Figure 4 shows the OFAT results from iterative creep modeling of blade geometries. Similar to the OFAT results, creep populations have a general decrease in frequency variation within the monte carlo design space population. Figure 5 shows the median frequency variations of the blade monte carlo design points, in those with and without creep.

The forward modeling results were imported into a virtual training set database for analysis using PCRT tools. Creation of virtual spectra (via superposition of lorentzian distributions) for each simulation also allows for a visual comparison of the model data and identification of trends. Figure 6 shows an example of seven virtual spectra created by successively increasing creep strain on each blade simulation. As creep strain increases, modes that are more sensitive to creep strain, such as Mode 15, shift more than others (for example, Mode 16 and 17). The same trend can be seen in the OFAT results presented in Figure 4.

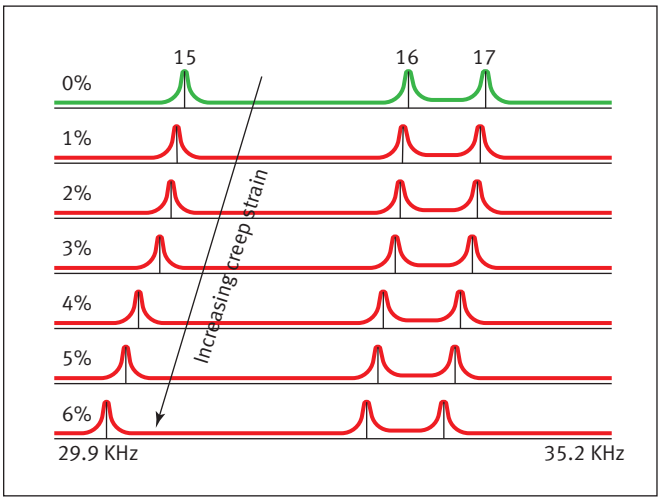

Figure 6. Virtual resonance spectra of modeled turbine blades with increasing creep strain.

FEM Grid Inversion

All creep inversion work presented in this section pertains to the 10 mm gage length SX dogbone as described in other scholarship (Biedermann et al., 2016). A gridded design space was created that varied 5 material parameters: elastic modulus (E_{001}), Poisson's ratio (ν_{001}), anisotropy ratio (A), crystal orientation (θ grain angle), and creep strain (Table 2).

Eight additional models were created to test the inversion code. The first four FEM design points, A, B, C, and D, varied material properties randomly from within the bounds of the gridded design space while the dimensions were fixed at nominal values to confirm that the inversion would converge to the correct values. Then four additional points, W, X, Y, and Z, were generated with random material and dimensional variations. These later points helped to examine the effects of normal dimensional variation on the inversion of creep.

Initial guesses of each parameter were fed into the inversion code for each of the 8 design points. The inversion code then used between 30 and 35 resonance peaks to estimate creep strain. Several inversions were performed on each design point using different starting guesses each time. Table 3 shows the known modeled creep strain, the best fit inverted estimate for creep strain, as well as the difference between them for each point. The error for samples A through D quantifies typical levels of uncertainty due to interpolation within the gridded design space and convergence of the inversion code. The larger error seen in samples W through Z reflects the additional uncertainty caused by dimensional variation. In order for the inversion code to estimate creep strain, other material properties of the samples had to be inverted. Table 4 shows the absolute material property values used in the modeling as well as the best fit inversion results. Overall, both the inversion of the creep and inversion of material properties were well matched to the known (modeled input) values.

TABLE 3
Inversion results of creep for modeled inputs

Sample		Modeled creep, %	Best fit, inversion creep, %	Difference
Material variation	A	1.33	1.17	–0.16
Material variation	B	2.67	2.55	–0.12
Material variation	C	5.33	5.40	0.07
Material variation	D	6.67	6.72	0.05
Material and dimensional variation	W	3.90	3.08	–0.82
Material and dimensional variation	X	1.30	1.42	0.12
Material and dimensional variation	Y	4.56	4.64	0.08
Material and dimensional variation	Z	6.12	5.70	–0.42

TABLE 4
Inversion results of material properties for modeled inputs

Sample		Modeled				Inversion best fit			
		E (GPa)	ν	A	$\theta°$	E (GPa)	ν	A	$\theta°$
Material variation	A	126.03	0.39	2.80	3.75	125.96	0.39	2.80	3.85
Material variation	B	126.88	0.36	2.84	6.25	126.88	0.36	2.84	6.16
Material variation	C	128.59	0.37	2.66	8.75	128.60	0.37	2.66	8.74
Material variation	D	129.44	0.38	2.71	1.25	129.46	0.38	2.71	1.18
Material and dimensional variation	W	125.76	0.36	2.84	0.72	125.74	0.36	2.84	0.00
Material and dimensional variation	X	128.91	0.36	2.82	6.80	128.82	0.36	2.83	7.08
Material and dimensional variation	Y	127.61	0.38	2.64	8.57	127.60	0.38	2.64	8.46
Material and dimensional variation	Z	130.14	0.39	2.69	2.64	130.21	0.39	2.68	2.51

VIPR Creep Correlation

The PCRT VIPR toolset generates statistical scores that are typically used for P/F NDE of components. VIPR scores can also be correlated to material conditions of interest in an inversion/characterization capacity. In this study, VIPR's ability to quantify the creep severity was explored.

For the dogbone geometries, VIPR used data from both the monte carlo forward models, as well as the grid-based models used initially for inversion. The monte carlo forward model and the grid-based inversion models had different nominal modeled material properties, as shown in Table 5. The differences could confound FEM inversion results, as the absolute frequency residuals are a key part of the convergence.

TABLE 5
Variation in the modeled material properties used for VIPR predictions

	E_{001} range	ν_{001} range	A range	θ range
Inversion grid	125 to 130 GPa	0.374 to 0.400	2.62 to 2.89	0 to 10°
Monte carlo study	110 to 114 GPa	0.316 to 0.329	3.00 to 3.14	0 to 12°

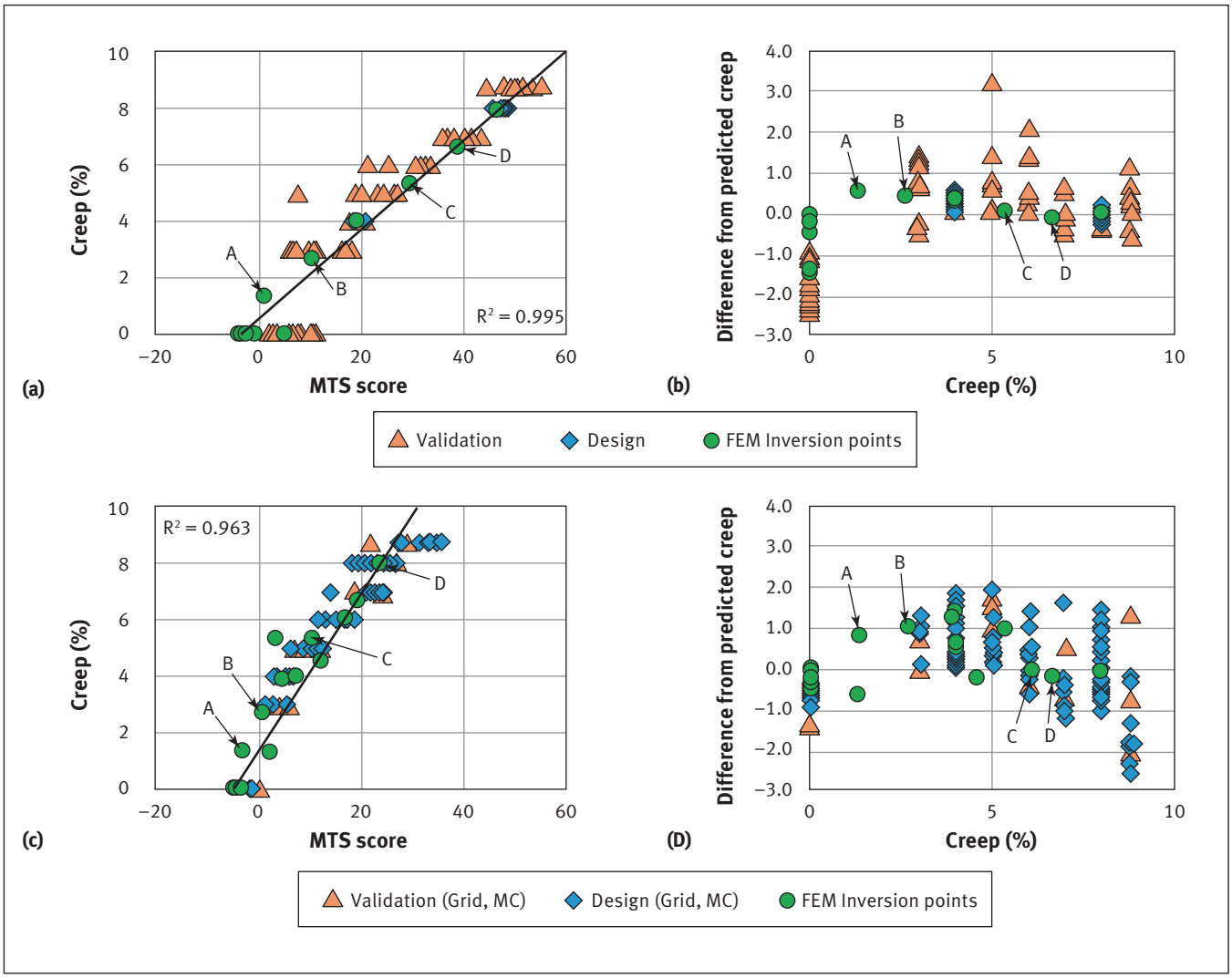

Figure 7. (a) Vibrational pattern recognition's correlation of mahalanobis-taguchi system to dogbone creep strain; (b) predictive ability of vibrational pattern recognition and inversion tools when trained with gridded inversion space data and validated with monte carlo forward model study data; (c) vibrational pattern recognition's correlation of to mahalanobis-taguchi system creep severity, and predictive ability; (d) when trained with a mix of gridded and monte carlo forward model study data.

However, VIPR finds optimal resonance patterns to diagnose the creep condition. The absolute frequency values are not as critical as the relational differences between frequencies.

As an initial test, the gridded data from the FEM inversion were used as the VIPR training set, and the forward monte carlo models were used as validation samples. The training set included over 115 undeformed samples and over 230 samples with creep. The validation set included more than 250 samples, with and without creep strain. In the initial test, VIPR was restricted to using the lower order modes (mode numbers 5 to 15). Modes below mode 5 were excluded because PCRT measurements showed the highest measurement error at the lowest modes, where the fixture's boundary conditions can have a measurable effect. Modes above mode 15 were excluded because mode-swapping in the modeled sets became more prevalent in that range.

VIPR solutions developed from the gridded model design set were evaluated and those with the best correlation between MTS score and creep were chosen. For the dogbones, the best VIPR correlation used 5 resonance modes, as opposed to the 30 to 35 used in the inversion space. These generated excellent predictions of creep levels for the validation monte carlo samples. The upper portion of Figure 7 shows a sample of these results. Figure 7a and 7b also highlights the inversion model design points A, B, C, and D. Figure 7c and 7d shows an alternate solution where parts from each the gridded and monte carlo data sets were used in the VIPR training set, with 15% of the data points overall excluded for validation.

For VIPR analysis of the blade geometries, only the monte carlo design spaces were used. The set included 149 samples without creep, and 43 samples with levels of creep strain ranging from 1.0% to 5.7%. Approximately 10% of the samples were randomly withheld for validation. VIPR solutions trained to the blades did not have as high a correlation between MTS score and creep strain as demonstrated by the dogbone samples, but the error between the actual creep values and the predicted creep values was comparable.

Figure 8 shows the results for the blade geometries correlating MTS score to creep. The lower correlation value, compared to the dogbones, may be due to the monte carlo blade population having a more complex geometry and larger geometric tolerances than those of the dog bone populations. A summary of all the VIPR creep predictions are shown in Table 6.

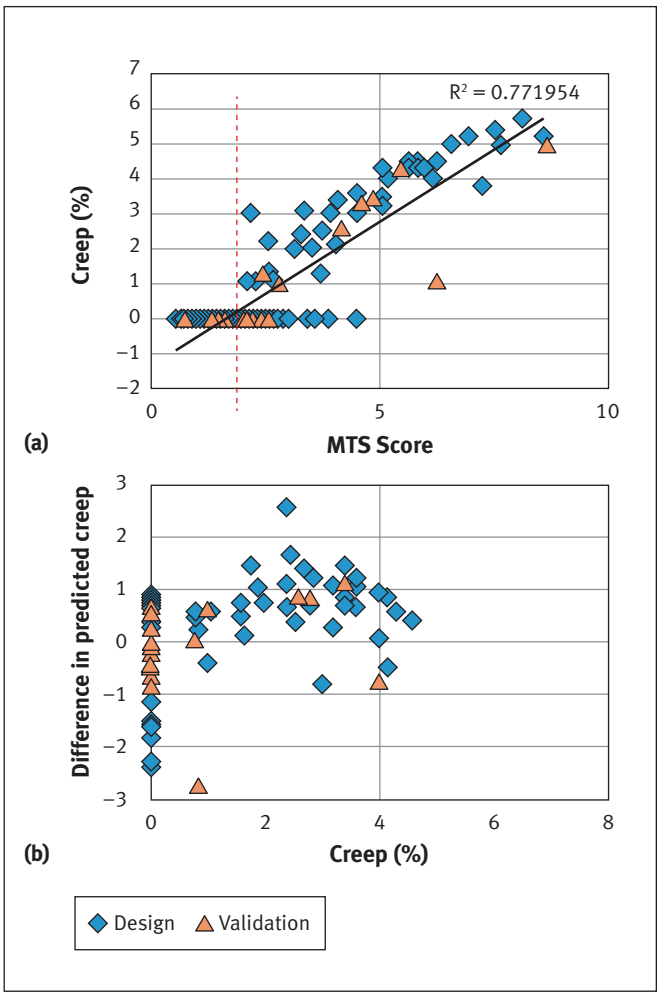

Figure 8. Vibrational pattern recognition's correlation of mahalanobis-taguchi system to: (a) creep severity; and (b) predictive ability, when trained with monte carlo forward model study data for blade geometry. The dashed line is the proposed mahalanobis-taguchi system limit.

TABLE 6
Results of vibrational pattern recognition predictions of creep

Part Geometry	Dogbone	Dogbone	Blade
Training/design data	Inversion grid	Grid, Monte carlo	Monte carlo study
Validation data	Monte carlo study	Grid, Monte carlo	Monte carlo study
Number of resonances in VIPR pattern	5	5	6
MTS-creep correlation	0.99	0.96	0.77
Maximum prediction in creep difference (design set)	0.57	2.67	2.6
Average predication in creep difference (design set)	0.0	0.0	0.0
Maximum prediction in creep difference (variation set)	3.2	2.18	2.7
Average prediction in creep difference (variation set)	−0.57	0.03	−0.01

TABLE 7
Inversion of material properties from measured data

Sample, measured creep strain, %	Inversion best fit			
	E (GPa)	ν	*A*	θ°
0	127.32	0.38	2.84	4.08
0.20	127.81	0.38	2.83	4.28
0.60	128.10	0.38	2.82	3.90
3.20	128.36	0.38	2.83	4.10
9.10	128.64	0.39	2.85	2.92

TABLE 8
Inversion and VIPR estimates of creep strain from measured data

Measured creep strain, %	VIPR estimate creep strain, %	VIPR difference	Inversion, best fit creep strain, %	Inversion error, difference
0.0	4.30	4.30	0.00	0.00
0.20	4.60	4.40	0.19	−0.01
0.60	4.80	4.20	0.59	−0.01
3.20	7.10	3.90	2.87	−0.33
9.10	13.60	4.50	9.13	0.03

VIPR sorting scores are also used to set limits for P/F-type sorting. In such an application, using the blade models as training data, an MTS cutoff would be selected that correlated to a worst allowable case level of creep strain (perhaps 2%). From Figure 8, the MTS cutoff to reject parts with less than 2% creep strain would be MTS = 2 (dashed line). Parts measured with an MTS score higher than two could be rejected from an overhaul process stream, or segregated for further evaluation.

Experimental Verification and Measured Data Inversion

A single-crystal dogbone was iteratively crept (as described earlier) and removed at intervals to make PCRT measurements. The PCRT model inversion methods were applied to the measured spectra for the crept dogbone. $E_{(001)}$, $\nu_{(001)}$, A, θ, and creep strain were inverted using the FEM approach, while the VIPR approach was used for a creep-only estimate. The inversion results for the material properties are shown in Table 7. The error between the measured and inverted values of creep are shown in Table 8. Figure 9 illustrates the differences between the known creep values and the inverted creep estimates for both modeled and measured data inversion inputs.

The inversion code had excellent estimations of creep strain in the measured and modeled data. The VIPR method showed high correlation in modeled data yet showed an offset between the estimated and measured creep strains. However, the offset of creep estimation was consistent (approximately 4%) across all creep levels, and the correlation trend agreed with the trend in the modeled data. VIPR currently examines the resonance patterns of a part relative to the entire trained population. Future work will evaluate VIPR results by comparing a part to itself, before and after service creep, to evaluate if the correlation between MTS and creep deformation can be improved. This verification demonstrates that both FEM and VIPR inversion can be trained through PCRT forward models to invert the quantity of creep damage in an SX dogbone.

In addition to estimating creep strain, the inversion code produced estimates of the material properties for the modeled and measured data. The true values of the measured data material properties are unknown and verification is needed to determine how close the inversion estimations are. To further evaluate the inversion results, FEM models were created using the best-fit inversion parameters of creep strain and material properties. Figure 10 compares the change in frequency from the undeformed state to 3% creep strain in the modeled and measured data. While a slight offset exists between the measured and modeled frequencies, the overall pattern is consistent because the measured and modeled mode sensitivities are the same. In fact, the measured creep data include a global frequency shift of approximately +0.3% after the first creep increment, which was not anticipated by the models. A similar anomalous global increase in resonance was reported after the first creep increment of polycrystalline superalloy dogbones by other authors, who postulate these observations may be due to changes in material microstructure or the residual stress state of the part (Goodlet et al., 2017).

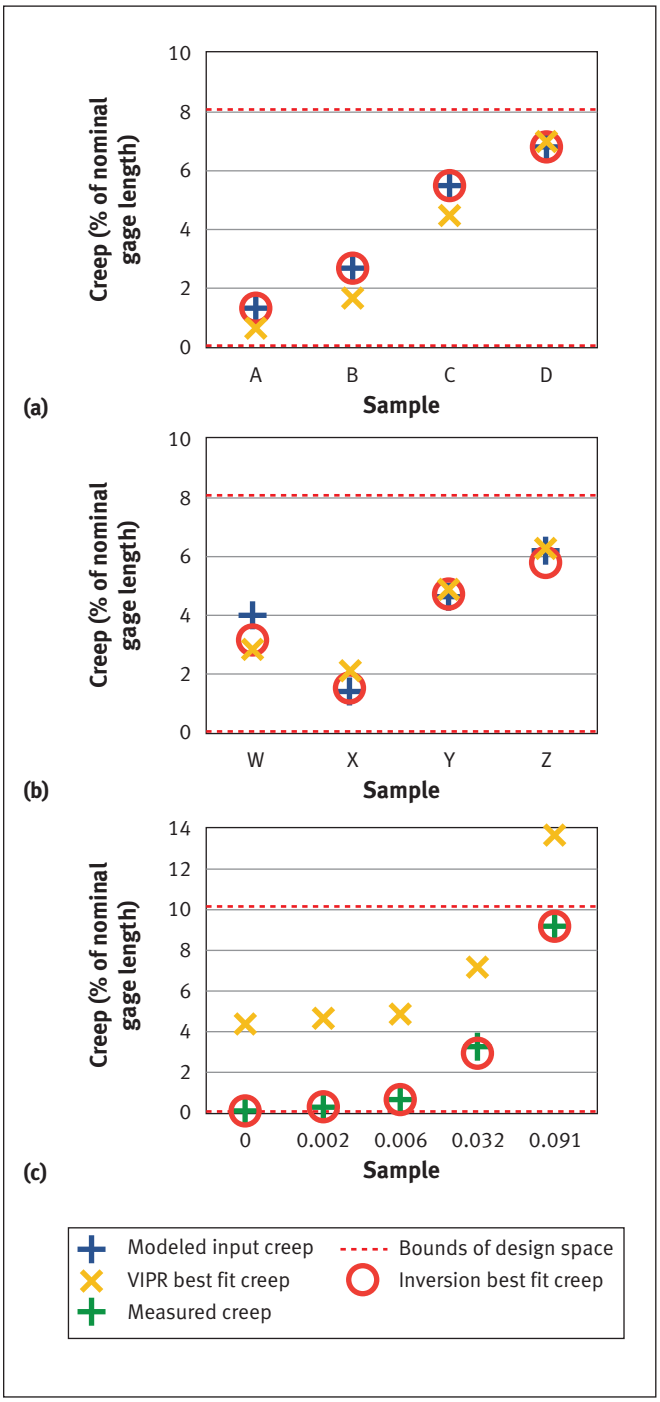

Figure 9. Plots of measured creep strain versus inversion estimates from (a) modeled data with material variation; (b) modeled data with material and dimensional variation; (c) measured data.

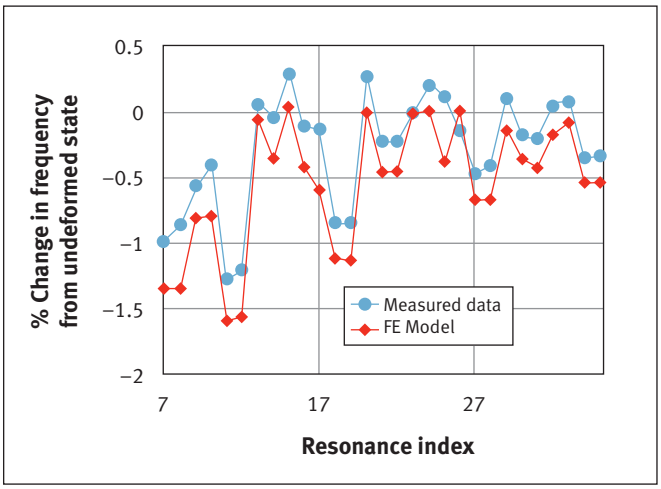

Figure 10. Frequency changes for 3% creep strain in measured data creep (solid line) and forward model based on inversion results (dashed line).

Conclusions and Future Work

This work demonstrates that a series of forward models can be used to train FEM inversion and VIPR algorithms to estimate the quantity of creep strain. Validation of forward models with experimental data showed the good model predictions of the resonance frequency changes in a range of creep strains. This work also shows that in modeled data, a part's resonant frequencies can be used to invert other material and geometric parameters that describe a part including $E_{(001)}$, $\nu_{(001)}$, A, and grain angle (θ). Ultimately, PCRT forward models and inversion can be expanded to include additional geometries, damage mechanisms, and inversion parameters. Future work will create and evaluate an inversion gridded design space for the SX blade geometries. Monitoring and measuring the change in resonance exhibited by a single part throughout its service life would allow the inversion process to focus on characteristics that have changed, without being confounded by sources of variation from the initial part state. For example, the primary grain angle affects resonance measurements, but does not change significantly during a service interval. Comparing a part to itself over time should therefore highlight the effects that damage accumulation has on resonance, while being immune to the natural parameter variation observed in a population of parts.

ACKNOWLEDGEMENTS

The authors wish to thank John Aldrin for his support during the course of this work. This research was supported by the US Air Force Research Laboratory (AFRL) through a Materials and Manufacturing Directorate (AFRL/RX) Structural Materials Broad Agency Announcement (BAA) Contract FA8650-15-M-5208 and an AFRL Small Business Innovation Research (SBIR) Phase II Contract, FA8650-15-M-5074. This paper has been cleared for public release by AFRL under case number 88ABW-2017-1323.

REFERENCES

ASTM, *ASTM E3081-16: Standard Practice for Outlier Screening Using Process Compensated Resonance Testing via Swept Sine Input for Metallic and Non-Metallic Parts*, ASTM International, West Conshohocken, Pennsylvania, 2016.

Biedermann, Eric, Leanne Jauriqui, John C. Aldrin, Brent Goodlet, Tresa Pollock, Chris Torbet, and Siamack Mazdiyasni, "Resonance Ultrasound Spectroscopy Forward Modeling and Inverse Characterization of Nickel-Based Superalloys," 41st Annual Review of Progress in Quantitative Nondestructive Evaluation: Vol. 34, Boise, Idaho, 20–25 July 2014, *AIP Conference Proceedings*, Vol. 1650, published online 2015.

Biedermann, Eric, Leanne Jauriqui, John C. Aldrin, Alexander Mayes, Tom Williams, and Siamack Mazdiyasni, "Uncertainty Quantification in Modeling and Measuring Components with Resonant Ultrasound Spectroscopy," 42nd Annual Review of Progress in Quantitative Nondestructive Evaluation:, Incorporating the 6th European-American Workshop on Reliability of NDE, Minneapolis, Minnesota, 26–31 July 2015, *AIP Conference Proceedings*, Vol. 1706, published online 2016.

Biedermann Eric, Julieanne Heffernan, Alexander Mayes, Garrett Gatewood, Leanne Jauriqui, Brent Goodlet, Tresa Pollock, Chris Torbet, John C. Aldrin, Siamack Mazdiyasni, "Process Compensated Resonance Testing Modeling for Damage Evolution and Uncertainty Quantification," 43rd Annual Review of Progress in Quantitative Nondestructive Evaluation: Vol. 36, Atlanta, Georgia, 17–22 July 2016, *AIP Conference Proceedings*, Vol. 1806, published online 2017.

Cudney, Elizabeth A., David Drain, Kioumars Paryani, Naresh Sharma, "A Comparison of the Mahalanobis-Taguchi System to A Standard Statistical Method for Defect Detection," *Journal of Industrial and Systems Engineering*, Vol. 2, No. 4, 2009, pp. 250–258.

Federal Aviation Administration (FAA), *AC 33.70-1: Guidance Material For Aircraft Engine Life-Limited Parts Requirements*, Advisory Circular No 33.70-1, Initialed by ANE-111, 2010 US Department of Transportation, Washington, DC, 2009.

Goodlet, B.R., C.J. Torbet, E.J. Biedermann, L.M. Jauriqui, J.C. Aldrin, T.M. Pollock, "Forward Models for Extending the Mechanical Damage Evaluation Capability of Resonant Ultrasound Spectroscopy," *Ultrasonics*, Vol. 77, 2017, pp. 183–196.

Grabcad, "CAD turbine blade model," accessed 17 May 2017 from https://grabcad.com/library/turbine-blade—4.

Jauriqui, Leanne and Lem Hunter, "A More Comprehensive NDE: PCRT for Ceramic Components," Review of Progress in Quantitative Nondestructive Evaluation: Volume 30AB, San Diego, California, 18–23 July 2010, API Conference Proceedings, Vol. 1335, published online 2011.

Migliori, A., J.L. Sarrao, William M. Visscher, T.M. Bell, M. Lei, Z. Fisk, and R.G. Leisure, "Resonant Ultrasound Spectroscopy Techniques for Measurement of the Elastic Moduli of Solids," *Physica B: Condensed Matter*, Vol. 183, No. 1–2, 1993, pp. 1–24.

Migliori, Albert and John L. Sarrao, *Resonant Ultrasound Spectroscopy: Applications to Physics, Materials Measurements, and Nondestructive Evaluation*, Wiley, New York City, New York, 1997.

Pastor M., Binda M., Harcarika T., "Modal Assurance Criterion" Procedia Engineering 48 (2012) 543-548**.**

Piotrowski, D., L. Hunter, and Trista Sloan, "Process Compensated Resonance Testing JT8D-219 1st Stage Blades," ATA NDT Forum 2008, (September 24, 2008). (http://www.vibrantndt.com/wp-content/uploads/75_2008_ATA_NDT_Forum-PCRT_of_JT8D-T1_Blades1.pdf).

Ramaglia, Alessandro D. and Paolo Villari, "Creep and Fatigue of Single Crystal and Directionally Solidified Nickel-base Blades via a Unified Approach Based on Hill48 Potential Function: Part 1 Plasticity and Creep," ASME Turbo Expo 2013: Turbine Technical Conference and Exposition, San Antonio, Texas, 3–7 June 2013.

Schwarz, Jim, Jay Saxton, and Leanne Jauriqui, "Process Compensated Resonant Testing in Manufacturing Process Control," *Material Evaluation*, Vol. 63, No. 7, 2005, pp. 736–739.

Taguchi, Genichi, Subir Chowdhury, and Yuin Wu, *The Mahalanobis-Taguchi System*, McGraw-Hill Professional, New York City, New York, 2001.